# Tailoring Hydrophobicity and Pore Environment in Physisorbents for Improved Carbon Dioxide Capture under High Humidity

Xiaoliang Wang<sup>1</sup>, Maytham Alzayer<sup>2</sup>, Arthur J. Shih<sup>3</sup>, Saptasree Bose<sup>1</sup>, Haomiao Xie<sup>1</sup>, Simon M. Vornholt<sup>4</sup>, Christos D. Malliakas<sup>1</sup>, Hussain Alhashem<sup>2</sup>, Faramarz Joodaki<sup>2</sup>, Sammer Marzouk<sup>1</sup>, Grace Xiong<sup>3</sup>, Mark Del Campo<sup>5</sup>, Pierre Le Magueres<sup>5</sup>, Filip Formalik<sup>2,6</sup>, Debabrata Sengupta<sup>1</sup>, Karam B. Idrees<sup>1</sup>, Kaikai Ma<sup>1</sup>, Yongwei Chen<sup>1</sup>, Kent O. Kirlikovali<sup>1</sup>, Timur Islamoglu<sup>1</sup>, Karena W. Chapman<sup>4</sup>, Randall Q. Snurr<sup>2\*</sup>, Omar K. Farha<sup>1,2\*</sup>

- 1 Department of Chemistry, Northwestern University, Evanston, Illinois 60208, United States
- 2 Department of Chemical & Biological Engineering, Northwestern University, Evanston, Illinois 60208, United States
- 3 Materials Science and Engineering, Northwestern University, Evanston, Illinois 60208, United States
- 4 Department of Chemistry, Stony Brook University, Stony Brook, New York 11794, United States
- 5 Rigaku Americas Corporation, The Woodlands, Texas 77381, United States
- 6 Department of Micro, Nano and Bioprocess Engineering, Wroclaw University of Science and Technology, 50-370 Wroclaw, Poland

\*Corresponding authors: Randall Q. Snurr – Email:  $\underline{snurr@northwestern.edu}$ ; Omar K. Farha – Email:  $\underline{o\text{-}farha@northwestern.edu}$ 

KEYWORDS: Metal-organic frameworks, CO<sub>2</sub> capture, Water competition, Physisorbent, Durability.

**ABSTRACT:** CALF-20, a Zn-triazolate-based metal-organic framework (MOF), is one of the most promising adsorbent materials for CO<sub>2</sub> capture. However, competitive adsorption of water severely limits its performance when the relative humidity (RH) exceeds 40%, limiting the potential implementation of CALF-20 in practical settings where CO<sub>2</sub> is saturated with moisture, such as post-combustion flue gas. In this work, three newly designed MOFs related to CALF-20, denoted as **NU-220**, **CALF-20M-w**, and **CALF-20M-e** that feature hydrophobic methyl-triazolate linkers are presented. Inclusion of methyl groups in the linker is proposed as a strategy to improve CO<sub>2</sub> uptake in the presence of water. Notably, both **CALF-20M-w** and **CALF-20M-e** retain over 20% of their initial CO<sub>2</sub> capture efficiency at 70% RH – a threshold at which CALF-20 shows negligible CO<sub>2</sub> uptake. Grand canonical Monte Carlo (GCMC) simulations reveal that the methyl group hinders water network formation in the pores of **CALF-20M-w** and **CALF-20M-e** and enhances their CO<sub>2</sub> selectivity over N<sub>2</sub> in the presence of high moisture content. Moreover, calculated radial distribution functions indicate that introducing the methyl group into the triazolate linker increases the distance between water molecules and Zn coordination bonds, offering insights into the origin of the enhanced moisture stability observed for **CALF-20M-w** and **CALF-20M-e** relative to CALF-20. Overall, this straightforward design strategy has afforded more robust sorbents that can potentially meet the challenge of effectively capturing CO<sub>2</sub> in practical industrial applications.

#### Introduction:

Due to the ability of carbon dioxide ( $CO_2$ ) to trap heat as a greenhouse gas, the accumulation of anthropogenic  $CO_2$  in the Earth's atmosphere from fossil fuel combustion is influencing the climate and contributing to the increasing frequency of natural disasters. As a result, the global community is seeking to reduce atmospheric carbon and achieve carbon neutrality in the next few decades. While renewable

energy sources have shown promise to limit CO<sub>2</sub> emissions, carbon capture has emerged as a critical and complementary strategy for mitigating carbon emissions and more rapidly addressing the wide-ranging impacts of climate change.<sup>3, 4</sup> Currently, multiple carbon capture technologies are available for capturing CO<sub>2</sub> from industrial processes, including pre-combustion capture, oxy-fuel combustion

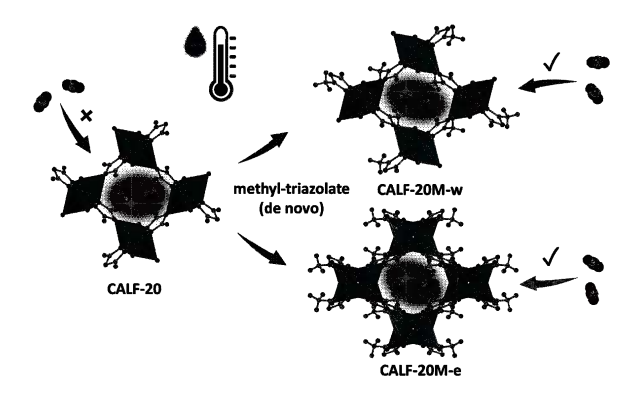
capture, and post-combustion capture, and each option exhibits distinct advantages and limitations.<sup>5, 6</sup> Among these approaches, post-combustion CO<sub>2</sub> capture methods have garnered the most attention,<sup>7</sup> primarily due to their adaptability, as these capture devices can be retrofitted into existing facilities.<sup>5</sup>

Solid adsorbents, such as porous carbons, zeolites, silicas, and resins, have shown promise as carbon capture materials<sup>8</sup> and demonstrated the ability to bind CO<sub>2</sub> through both physisorption and chemisorption.<sup>7</sup> Although chemisorption, for example with amines, often has high selectivity, in most instances, CO<sub>2</sub> chemisorbents bind CO<sub>2</sub> quite strongly, creating a high energy penalty for the regeneration of the material.9, 10, 11 In contrast, physisorbents require less energy for regeneration, and the challenge is to find materials with good selectivity and capacity. There are suggestions in the literature that physisorbents with moderate CO2 selectivity and uptake are promising for industrial-scale CO<sub>2</sub> capture. 12-14 However, in addition to capacity and selectivity, the material must also exhibit high stability in the presence of water, as many CO<sub>2</sub> point sources contain high moisture content. Among the many adsorbents considered to date for CO<sub>2</sub> capture, metal-organic frameworks (MOFs) have shown great promise, since these porous crystalline structures are highly tunable, offering control over properties such as pore volume, surface area, and surface chemistry for CO<sub>2</sub> capture applications. 7, 9, 15-21

Recently, a Zn-triazolate-based MOF known as CALF-20, has shown great promise as a CO<sub>2</sub> physisorbent, as it demonstrates selective CO<sub>2</sub> capture, high CO<sub>2</sub> capacity, rapid kinetics, and requires modest energy for regeneration.<sup>22, 23</sup> In fact, the Canadian company Svante is now employing CALF-20 in their carbon capture process.<sup>24</sup> However, the CO<sub>2</sub> adsorption capacity of CALF-20 is significantly compromised at high relative humidity (RH) values, and water uptake begins to surpass CO<sub>2</sub> uptake at 40% RH.<sup>22, 25</sup> As a result, CALF-20 is unsuitable for direct use in carbon capture settings where water saturation is prevalent, such as wet flue gas conditions, and requires an initial dehydration step (e.g. compressor inter-stage cooling, guard-beds of solid desiccants, liquid desiccants) that adds complexity and reduces the overall process efficiency. 26-28 We hypothesized that incorporating hydrophobic groups, such as a methyl (-CH<sub>3</sub>) group, into the triazolate linker of CALF-20 would enhance its CO<sub>2</sub> capture performance at high RH values. In addition, we envisioned that replacing the hydrogen atom on the 3position of the 1,2,4-triazole (ta) ring with a methyl group would increase the water stability of this material, resulting in a material with better CO2 adsorption properties and better stability (Scheme 1).

Using this strategy, we synthesized three distinct MOFs using the 3-methyl-1H-1,2,4-triazole (mta) linker and zinc oxalate (ZnOx) and found that the solvent and reaction conditions determine the structure of the MOF product. While methanol-assisted synthesis results in a novel MOF, denoted as NU-220, reactions performed in water or ethanol afford CALF-20M-w and CALF-20M-e, respectively, which are both isostructural to CALF-20. Notably, these materials exhibit between 1.81 and 2.13 mmol g<sup>-1</sup> CO<sub>2</sub> uptake at 0.15 bar (i.e., the typical CO<sub>2</sub> partial pressure in flue gas), which corresponds to 69-78% of the capacity of CALF-20 at this pressure, confirming that introducing the methyl group does not significantly decrease the CO<sub>2</sub> uptake capacity.

Importantly, at the high RH value of 70%, CALF-20M-w and CALF-20M-e maintain approximately 0.5 and 0.6 mmol  $\rm g^{-1}$  of CO<sub>2</sub> capture capacity, respectively, whereas CALF-20 demonstrates no CO<sub>2</sub> uptake under these conditions, entirely compromising its carbon capture capability. In this work, experimental and computational studies show how differences in the MOF structures result in distinct differences in performance for CO<sub>2</sub> capture in both dry and humid environments. More broadly, this work indicates that these new methyl-triazolate-based sorbents are more suitable for post-combustion carbon capture applications that contain high humidity than their non-methylated counterpart.



**Scheme 1.** Enhancement of CO<sub>2</sub> capture under high relative humidity with **CALF-20M-w** and **CALF-20M-e** via modification of CALF-20 with a hydrophobic methyl group.

#### **Results and discussion**

## Synthesis and Structural Characterization

To begin our investigation, we screened the reactions of mta with ZnOx in different solvents. The individual components were pre-mixed in methanol, ethanol, or water separately and heated at 180 °C for 3 days in a Parr vessel (see supporting information for details). Similar to the synthesis of CALF-20, all three reactions generate a white material that precipitates out. Interestingly, powder X-ray diffraction (PXRD) analysis of the products indicates each of the three solvents produces a different crystalline material, which contrasts the behavior of CALF-20, as the same phase-pure sample can be synthesized from either methanol or ethanol.<sup>22</sup> The new polymorphic phases isolated from methanol and water, which we denoted as NU-220 and CALF-20M-w, were further characterized by single crystal X-ray diffraction (SCXRD) analysis (vide infra). Despite repeated attempts to produce a single crystal of the polymorphic phase isolated from ethanol, CALF-20M-e, we were unable to synthesize a crystal that was suitable for SCXRD analysis. However, we successfully employed microcrystal electron diffraction (MicroED) to obtain and refine the structural parameters of CALF-20M-e (crystal data in Table S1). Fig**ure 1** illustrates the structures of these three new MOFs, as well as the structure of CALF-20.

CALF-20, which has a structural formula of  $[Zn(ta)(ox)_{0.5}]$ , is composed of layers of zinc (II) ions that are connected by oxalate ions and triazolate units (**Figure 1b**). The Zn(II) center is five-coordinate and has a distorted trigonal bipyramidal geometry with Zn-O distances of 2.022(2) and 2.189(3) Å and Zn-N distances of 2.007(2), 2.016(3), and 2.091(3) Å (**Table S2**).<sup>22</sup> The N atoms in the 1,2 positions of the triazolate linker bridge Zn dimers, which are linked to

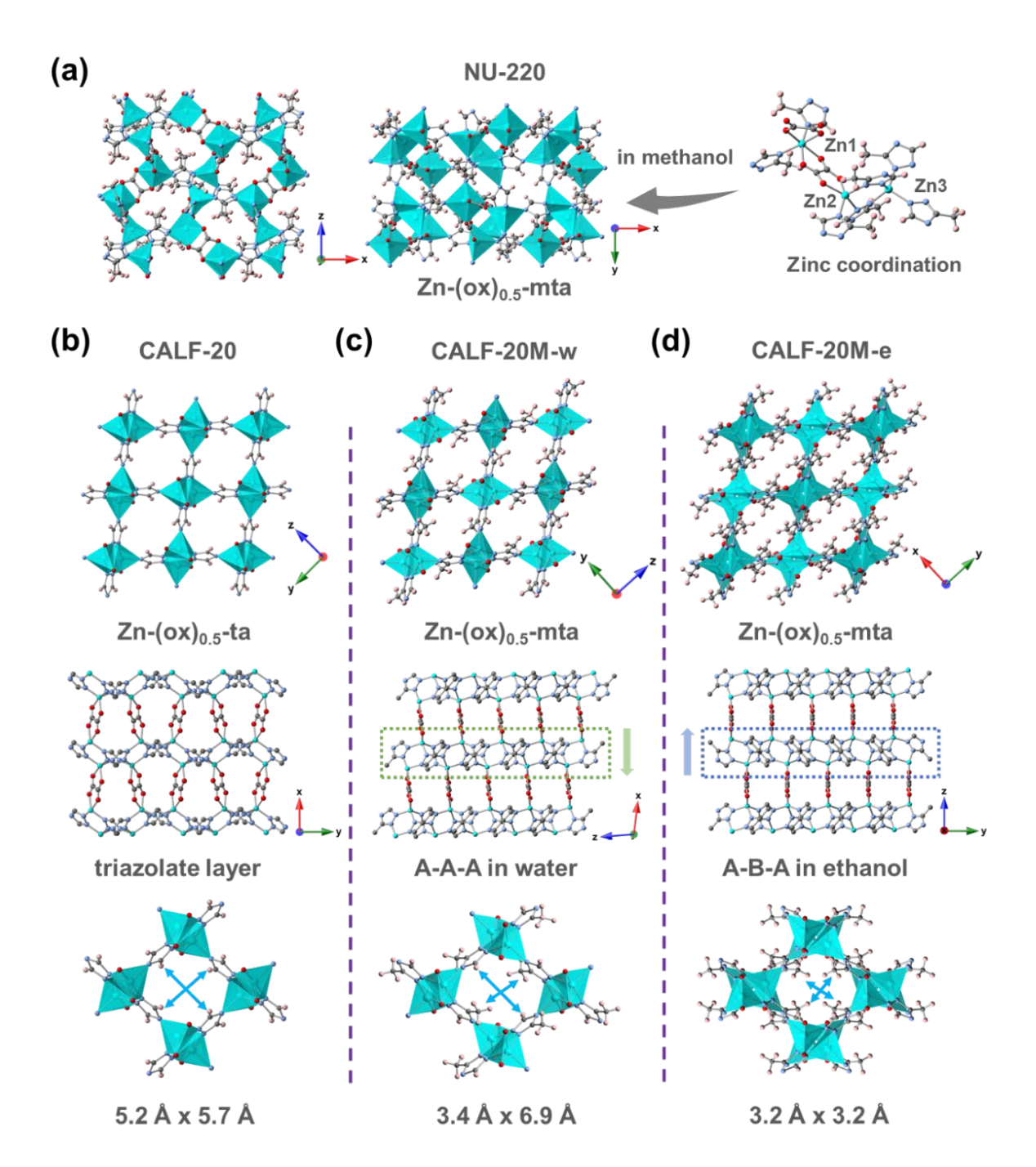


**Figure 1.** (a) Structure of **NU-220** and view of the zinc coordination. Crystal structures of (b) CALF-20 (c) **CALF-20M-w** and (d) **CALF-20M-e**, including the structure of zinc-triazolate layer, orientation of each layer pillared by oxalate and corresponding single pore channel. Color scheme (C: grey; N: blue; O: red; Zn: cyan; H: pink)

the next dimer by the N atom in the 4-position. The Zn coordination is completed by two oxygen atoms of a chelating oxalate group, and there are no open coordination sites. Following the reaction in methanol, NU-220 crystalizes in the tetragonal space group  $P4_32_12$  (Figure 1a) with a formula of [Zn(mta)(ox)<sub>0.5</sub>] and novel topology (Figure S1) that differs from the monoclinic  $P2_1/c$  system known for CALF-20. NU-220 has three types of zinc moieties (Figure S2 and Table S2): 1) hexa-coordinated zinc where the metal center is connected with two triazolate linkers and two cis-oxalate linkers (Zn-O = 2.093(4) and 2.189(4) Å; Zn-N = 2.090(5); Å; 2) penta-coordinated zinc (similar to that found in CALF-20) where it is connected with three triazolate linkers (Zn-N = 2.034(5), 2.036(4) and 2.122(4), and one bridged

oxalate linker (Zn-0 = 2.038(4) and 2.085(4) Å); 3) tetracoordinated zinc that is connected to four triazolate linkers (Zn-N = 1.983(5) and 2.022(4) Å.

In contrast, reactions in water and ethanol lead to the formation of **CALF-20M-w** and **CALF-20M-e**, respectively, which crystalize in the monoclinic P2<sub>1</sub>/c and orthorhombic Pbcn space groups with a formula of [Zn(mta)(ox)<sub>0.5</sub>] (**Figure 1c-d**). Both MOFs exhibit penta-coordinated zinc ions in a distorted trigonal bipyramidal geometry (**Figure S3**), similar to the zinc ions in CALF-20. The Zn-O distances in **CALF-20M-w** are 2.026(3) Å and 2.176(3) Å, while the Zn-N distances span 2.108(3) Å, 2.016(3) Å, and 2.037(3) Å. Similarly, **CALF-20M-e** features Zn-O distances of 2.00(5) Å

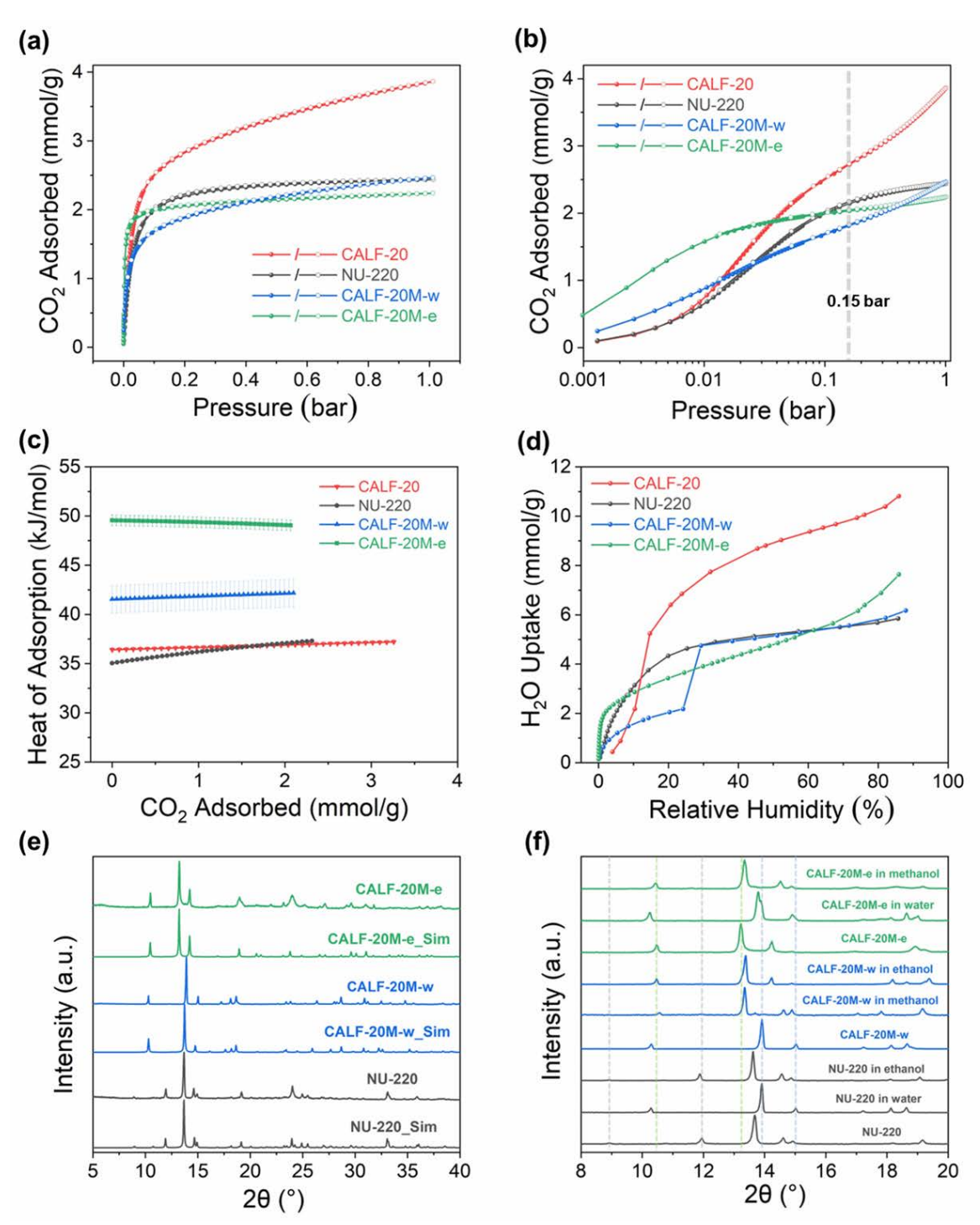


**Figure 2.** Sorption isotherms and PXRD for CALF-20, **NU-220**, **CALF-20M-w** and **CALF-20M-e**: (a-b) CO<sub>2</sub> isotherms at 298 K and (d) water isotherms at 298 K. (c) Heat of adsorption of CO<sub>2</sub> of all sorbents obtained from CO<sub>2</sub> isotherms at 273 K, 298 K and 313 K. (e) PXRD of simulated and as-synthesized sorbents. (f) PXRD profiles relevant to phase transition after boiling in different solvents (water, methanol and ethanol) at 453 K for 24 hours.

and 2.12(3) Å and Zn-N distances of 1.99(5) Å, 2.05(5) Å, and 2.12(4) Å (**Table S2**). Although the space group and unit formula of **CALF-20M-w** resemble those of CALF-20, the structure of **CALF-20M-w** differs slightly. For instance, due to the steric hindrance of the methyl group in **CALF-20M-w**, the interplanar angle between the oxalate group and the  $Zn_2(ta)_2$  moiety is higher (63.65°) compared to the analogous angle in CALF-20 (50.85°) (**Figure S4**), making **CALF-20M-w** a unique isomer of CALF-20. Such a distortion is common for molecular trigonal bipyramidal complexes.<sup>29</sup>

Structural analysis of **CALF-20M-w** and **CALF-20M-e** unveiled noteworthy alterations in the pore properties relative to those of CALF-20 that arise from the presence of the methyl groups that line the pores. Specifically, the pore apertures for **CALF-20M-w** and **CALF-20M-e** are 3.4 Å  $\times$  6.9 Å and 3.2 Å  $\times$  3.2 Å, respectively, which are significantly reduced from the pore aperture of 5.2 Å  $\times$  5.7 Å found in CALF-20. Notably, the structures of **CALF-20M-w** and **CALF-20M-e** differ from one another in the orientation of the layers within each material. The triazolate layers in **CALF-20M-w** exhibit a unidirectional arrangement, denoted as A-A-A,

while those in **CALF-20M-e** display an alternating orientation pattern of A-B-A. This difference in layer orientation further impacts the dimensions of the pore channels, resulting in a smaller effective 1D channel and 18% reduction of unit cell volume for **CALF-20M-e**. In contrast, the triazolate layer in CALF-20 and its hydrated form do not adopt a similar configuration.<sup>30-32</sup> As three different structures with the same linker were obtained by only varying the solvents used in the synthesis, it can be assumed that different solvents interact with MOF precursors and significantly influence the nucleation, crystal growth, and self-assembly processes involved in the synthesis.

# Irreversible Solvent-dependent Phase Transitions of Polymorphs

To investigate phase transitions among the three polymorphs, we incubated the corresponding MOFs (~50 mg) at 453 K for 24 hours in two alternative solvents (10 mL) separately and observed the dynamic response of the framework to solvent stimuli (e.g., methanol-synthesized NU-220 incubated in water and ethanol separately), highlighting the pivotal role of solvents in directing the structure from thermal kinetics aspects. We monitored the phase transitions using PXRD (Figure 2f). Notably, incubating NU-220 in water at 453 K afforded a phase transition into CALF-20M-w, but this transition was not observed upon incubation of NU-220 in ethanol under otherwise analogous conditions (Figure S5-7). This phase transition is found to be irreversible, as incubating CALF-20M-w in methanol at 453 K for 24 hours fails to induce the transformation back to the NU-220 phase (Figure S5). However, incubating CALF-20M-w in ethanol results in an unexpected transition to a new phase that exhibits slight differences from CALF-20M-e, as evidenced by variations in peak positions in the PXRD patterns (**Figure S7**). Specifically, the  $2\theta$  values of peaks originally located at 10.3°, 13.9°, and 15.0° in CALF-20M-w shift to 10.5°, 13.4°, and 14.2°, respectively, and the peak at 13.2° in **CALF-20M-e** is absent from the pattern for the new material. Nevertheless, upon analyzing the CO<sub>2</sub> isotherms, it is evident that the similarity in shape and trend closely aligns with that observed in CALF-20M-w (Figure S8), suggesting that ethanol initiates structural transformations, but these ethanol-induced changes are insufficient to fully reorient the triazolate-layer to match the orientation observed in CALF-20M-w. A similar phenomenon was observed after incubating CALF-20M-e in water, supporting an irreversible transition to CALF-20M-w (Figures S6 and S8).

The effects could encompass diverse mechanisms, including lattice swelling or contraction, solvent coordination, and hydrogen bonding. We hypothesize that during the synthesis of **CALF-20M-e**, the solvent ethanol serves as a template and fills the voids within the structure. However, the ultramicroporous space of CALF-20M-w limits the diffusion of ethanol, thereby hindering its phase transition to CALF-**20M-e**. The results suggest that a potential energy barrier inhibits the reversal of the triazolate layers from the A-B-A pattern in CALF-20M-e to the A-A-A pattern in CALF-20Mw. Variations between solvents, including differences in polarity, coordinating abilities, and hydrogen bonding capabilities, afford varying effects on the coordination environment, intermolecular interactions, and packing arrangements within the MOF structure.33 In these materials, solvents interact with the structural components to induce

alterations in the packing arrangement and bonding interactions, resulting in a dynamic response at elevated temperatures. For instance, methanol displays intermediate polarity and molecular size in comparison to water and ethanol. The presence of a larger dipole moment and fewer carbon atoms in methanol results in stronger hydrogen bonding and dipole-dipole interactions compared to ethanol. The same phase products were observed in propanol (1-proponal and isopropanol) and butanol (Figure S9), and a binary mixture of water and ethanol resulted in an A-A-A pattern like CALF-20M-w.34 Methanol potentially serves as a template with proper molecular dimension for the growth of the framework around methanol molecules in NU-220. Overall, these experimental findings suggest that the solvent not only has effects during the nucleation, crystal growth, and self-assembly processes, but also contributes to the phase transition behavior of these MOFs under different media.

### Analysis of Pure Gas and Vapor Adsorption.

We then collected CO<sub>2</sub> sorption isotherms for NU-220, CALF-20M-w, CALF-20M-e, and CALF-20 at 298 K and observed that the shape of the CALF-20M-w isotherm closely resembles that of CALF-20, while the isotherms of NU-220 and CALF-20M-e feature slightly different shapes based on the slope of the plateau region (Figure 2a). Notably, the CO<sub>2</sub> isotherm for CALF-20M-w exhibits an uptake of 1.0 mmol g-1 at 13 mbar, which is comparable to that of CALF-20 at this pressure, but the CALF-20M-w isotherm is shifted downward at higher pressures compared to the CALF-20 isotherm due to the reduced total pore volume (Figure 2b). Interestingly, CALF-20M-e demonstrates the highest CO<sub>2</sub> adsorption of ~1.87 mmol g-1 among the four sorbents at low  $CO_2$  concentrations of  $\sim 0.03$  bar, and it reaches a plateau of 2.05 mmol g-1 at 0.15 bar. The calculated heats of adsorption (Q<sub>st</sub>) of approximately 35-50 kJ mol<sup>-1</sup> for CALF-20, NU-220, CALF-20M-w and CALF-20M-e indicate that physisorption plays a dominant role in the CO<sub>2</sub> capture mechanism (**Figure 2c**). The O<sub>st</sub> values were calculated based on three isotherms at 273, 298 and 313 K and fitted with the virial method (Figure S10-17). Among these four adsorbents, **CALF-20M-e** exhibits the highest calculated Q<sub>st</sub> value of 50 kJ mol<sup>-1</sup>, indicating this MOF features the strongest interactions for CO<sub>2</sub> capture among this series. The experimentally observed trend for Q<sub>st</sub> values (CALF-20M-e > **CALF-20M-w** > **NU-220** ≈ CALF-20) matches well with the sequence of adsorption energies calculated by finding the minimum energy for a single adsorbate molecule in the MOFs using a classical force field (**Table 1**). Notably, we observed that the CO2 isotherms in NU-220 and CALF-20M-e reach saturation before 0.2 bar, while the CALF-20 and **CALF-20M-w** isotherms continue to rise over the pressure range we studied. Furthermore, we observed that for CALF-20M-e the isotherms at 313 K and 298 K exhibit a plateau (Figure S16), but when the temperature is decreased to 273 K, the CO<sub>2</sub> isotherm does not plateau and exhibits a gradual increase in CO<sub>2</sub> uptake up to 1 bar, suggesting structural flexibility and a variation in the adsorption mechanism (Figure S16), which is not observed in NU-220 (Figure \$12).

Next, we obtained  $H_2O$  sorption isotherms at 298 K for CALF-20, NU-220, CALF-20M-w, CALF-20M-e, with the results presented in Figure 2d. The water isotherm in CALF-

20 exhibits an inflection point around 10% RH and has the highest uptake at higher RH, approaching ~8 mmol/g at 35% RH. **NU-220** reaches ~5 mmol/g of water sorption at approximately 20% RH, with a more gradual increase at higher RH. CALF-20M-w and CALF-20M-e generally exhibit lower water uptake than CALF-20 at RH, suggesting a diminished affinity between water and the sorbent pores at high loading. At very low RH (below 10% RH), however, the three new polymorphs actually show higher water uptake than CALF-20. From the viewpoint of surface chemistry, the methyl group in the mta linker of NU-220, CALF-20M-w and CALF-20M-e should increase the hydrophobicity of the pores relative to that of the non-methylated linker in CALF-20, and indeed this was our initial motivation for including methyl groups. It is, thus, somewhat surprising that the isotherms in Figure 2d show that the new MOFs containing methyl groups exhibit higher water adsorption than CALF-20 at low RH. The surprising increase in hydrophilicity (higher water uptake at low RH) of the methyl-containing MOFs seen in Figure 2d is consistent with the water adsorption energies calculated from atomistic modeling in Table 1.

Table 1. Adsorption energy of a single adsorbate molecule (kJ/mol) after energy minimization utilizing classical force field and experimental heat of adsorption (Q<sub>st</sub>) for all four sorbents.

Structure	Qst (CO <sub>2</sub> )	CO <sub>2</sub>	H <sub>2</sub> O	N <sub>2</sub>				nperatures and high Ri erated aging (SAA) ex
(a) _				50	(b)			
ලි 2.5 -				2000000			* CALF-20M-w	# Silicon
2.0 -	- CONTROL	90000000000	0000000000		~		<u></u>	SAA-15D/Silicon
) ped 1.5	A SECTION OF THE PROPERTY OF T	/-	CALF-2 SAA_7	D	y(a.u		<u></u>	SAA-7D/Silicon
CO <sub>2</sub> Adsorbed (mmol/g)	Section Sectio	<b>→</b> /-	SAA_1	5D	Intensity(a.u.)		<u> </u>	SAA-2D/Silicon
ن 0.0-	Ī	A'					<u></u>	CALF-20M-w/Silicon
(c)	0.0 0.2 P	0.4 ressure	0.6 0.8 (bar)	1.0	(d)	10	15 20 2 2θ (°	5 30 35 40
I	SA	istine AA_7days	SAA_2 da SAA_15 d	ays			ļ	
Crystallinity (%)	93 92	100 101 97	93	97 92	(i.		1	6
nity					Intensity (a.u.)		1	- 5
stalli					ensit			
C					Inte			
						<u> </u>	<del></del>	
0+	NU-220	CALF-20	M-w CA	LF-20M-e	5	10	15 20 2 2θ (°)	25 30 35 40

**Figure 3.** (a)  $CO_2$  isotherms at 298 K and (b) PXRD of **CALF-20M-w** before and after aging at 343 K, 80% RH for 7 and 15 days. Silicon was mixed with the sorbent to quantitatively analyze variations in intensity from characteristic peaks. (c) Crystallinity changes after SAA experiments at 343 K, 80% RH for 2, 7, 15 days compared to the pristine samples. (d) VT-PXRD for **CALF-20M-w** from 298 to 623 K. The temperature ramp was set to 5 K min<sup>-1</sup>, holding for 5 min at each set point.

CALF-20	36.8 (±0.2)	-39.9	-42.1	-22.4
NU-220	36.3 (±0.1)	-44.1	-49.1	-24.5
CALF-20M-w	41.9 (±1.4)	-48.6	-50.9	-24.8
CALF-20M-e	49.3 (±0.5)	-53.0	-50.9	-25.3

From the single-component  $CO_2$  and water isotherms, we see that the reduced pore sizes of **CALF-20M-w** and **CALF-20M-e** enhance both the  $CO_2$  and  $H_2O$  uptake at low pressures. The minimal  $N_2$  adsorption at 77 K in **CALF-20M-w** and **CALF-20M-e** (**Figure S18**) is consistent with smaller pores. However, as we show below, for multicomponent adsorption, **CALF-20M-w** and **CALF-20M-e** suppress adsorption of water in mixtures with  $CO_2$  and  $N_2$ .

# Accelerated Aging and Thermal Stability Characterization.

The stability and regenerability of  $CO_2$  sorbents are critical factors in their suitability for operational conditions and efficient  $CO_2$  capture in flue gas systems. Long-term stability is paramount to ensure the extended lifespan of sorbents, including in the presence of competing gases and vapors. To evaluate the stability of the activated samples under harsh conditions of elevated temperatures and high RH, we conducted standardized accelerated aging (SAA) experiments.

Specifically, we incubated the activated sorbents in a humidity oven at 343 K and 80% RH for 15 days to accelerate the aging process. To evaluate the degradation rate of sorbents, we re-activated the aged samples and measured their  $CO_2$  sorption isotherms after 7 and 15 days. It was found that all three sorbents exhibit consistent  $CO_2$  isotherms throughout the aging process, confirming their stability (**Figure 3a and S20-22**).

Additionally, we performed a quantitative analysis of PXRD patterns to directly assess the changes in crystallinity utilizing silicon as an internal standard (Figure S23 and Table **S3**). Specifically, we evaluated the ratio of peak intensities (R = p1/p2), where p1 represents the intensity of the selected characteristic peak of the sorbent and p2 corresponds to the intensity of silicon. (In pure silicon, both p1 and p2 represent two different peaks from silicon.) To account for potential fluctuating mass effects on diffraction intensity, a small portion of the sample was taken from the pre-mixed samples for PXRD during SAA experiments. To quantify the crystallinity changes, we selected the characteristic peaks of **NU-220** at 13.66° {201} (**Figure S24**), CALF-20M-w at 13.91° {001} (Figure 3b), CALF-20M-e at 13.79° {110} (Figure S25) for the sorbents (p1), and 28.52° {111} (p2) for silicon, respectively. The results provided comparable R values for the characteristic diffraction peaks in all three aged sorbents, indicating unchanged crystallinity. R values for NU-220, CALF-

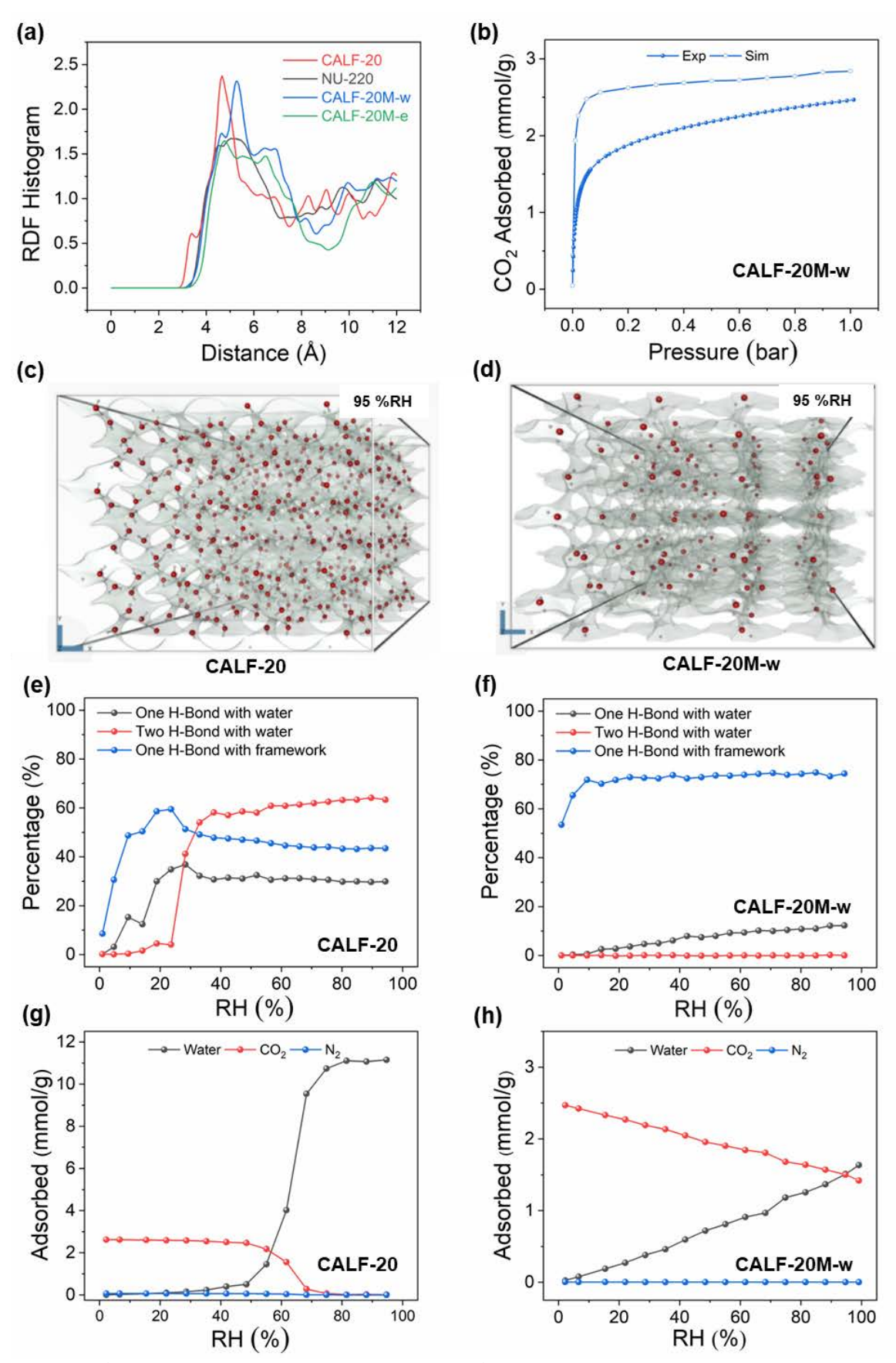


**Figure 4.** Results from GCMC simulations. (a) Radial distribution functions (RDF) between the Zn-N bond and the water molecules in four sorbents. (b) Comparison of experimental and simulated CO<sub>2</sub> isotherms at 298 K in **CALF-20M-w**. (c-d) Configurations of water molecules at 95% RH from single-component simulations (Color code. 0: red, c: grey, frameworks shown in transparent gray) and (e-f) percentage of water molecules with one or two H-bonds with other water molecules and one H-bond with the framework in CALF-20M-w. (g-h) Simulated competitive isotherms for CO<sub>2</sub>, water and N<sub>2</sub> at 298 K for CALF-20M-w.

**20M-w** and **CALF-20M-e** fluctuate in the range of 0.84-1.00, 0.89-0.97 and 0.33-0.37, respectively (**Table S3**). We evaluated the crystallinity ( $R/R_0$ , where  $R_0$  represents the R value before aging) of each material based on the relative R values and found that for all cases, the quality of each crystalline structure shows only negligible degradation (**Figure 3c**). We then employed scanning electron microscopy (SEM) to corroborate these observations, and we verified that minimal changes in particle size and morphology occur following the aging measurements (**Figure S26**), further supporting the remarkable stability of three sorbents under the specified conditions.

Following SAA stability assessments, we shifted our attention to probing the thermal stability of NU-220, CALF-20Mw, and CALF-20M-e and conducted variable-temperature PXRD (VT-PXRD) measurements from 298 to 673 K. Remarkably, NU-220 and CALF-20M-w preserved their structural integrity up to 648 K (Figures S27and 3d), while **CALF-20M-e** undergoes a loss of crystallinity at 623 K (**Fig**ure \$28). The results align well with the findings from the thermal gravimetric analysis (TGA) (Figures S29-31), where sorbents start losing weight around 623 K under both N2 and air. Moreover, the VT-PXRD analysis of CALF-**20M-w** reveals distinctive evidence of structural flexibility. as some of the peaks shift positions—a phenomenon absent in NU-220 (Figures S32-34). For instance, the characteristic peaks at 10.31° {110} and 13.69° {011} shift to 10.58° and 13.63° at 448 K, indicating a variable unit cell at elevated temperature (Figure S33). This is also observed in CALF-20M-e where the peaks shifted from 23.87° to 23.53° (Figure S34). To better assess the chemical stability under practical conditions, such as exposure to acidic gases (typically <500 ppm), the sorbents were subjected to high concentrations of NO<sub>X</sub> and SO<sub>2</sub> (1 bar) for three hours. PXRD profiles affirmed that their crystallinity remained unchanged. (Figures S35-37) Both NU-220 and CALF-20M-e displayed identical CO<sub>2</sub> adsorption isotherms at 298 K (Figures S38 and S40), while CALF-20M-w exhibited a slightly reduced capacity (~2%. Figure S39). Overall, these experiments demonstrate the high thermal and chemical stability of these materials.

## **Modeling analysis**

To better understand the behavior of these MOF sorbents, we performed grand canonical Monte Carlo (GCMC) simulations (see **Supporting Information** for details). First, to elucidate the demonstrated robustness under SAA conditions, we simulated pure water adsorption and examined the distribution of water molecules within the framework. The distance between the Zn-N bonds and adsorbed water molecules was quantified by the radial distribution function (RDF) at 95% RH. As illustrated in Figure 4a, CALF-20 shows the minimal distance (<4.0 Å) between water and the Zn-N bond, suggesting a heightened likelihood of water disrupting the Zn-N bond through substitution. Conversely, we observed shortest distances greater than 4 Å in NU-220, **CALF-20M-w**, and **CALF-20M-e**. Although a distance of  $\sim$ 3 Å is insufficient to form a Zn-water coordination bond in CALF-20, the incorporation of bulky methyl groups into the triazolate linkers further impedes water proximity to Zn-N bonds, thereby bolstering the framework's robustness to a higher level.

The minimum interaction energy between a single molecule (CO<sub>2</sub>, H<sub>2</sub>O<sub>1</sub> or N<sub>2</sub>) and each sorbent was calculated using the same force field as used for the GCMC simulations (modelling details in Supporting Information). As shown in Ta**ble 1**, N<sub>2</sub> has a very similar interaction energy with all four sorbents, whereas water has similar interaction energies (around -50 kJ/mol) with NU-220, CALF-20M-w, and **CALF-20M-e** but a less favorable interaction (-42.1 kJ/mol) with CALF-20. Given that the newer adsorbents contain methyl groups - which were added due to their supposed hydrophobicity - this is surprising. However, as noted above, the results are consistent with the low-pressure trends in the experimental water isotherms (Figure 2d). For CO<sub>2</sub>, the interaction energies increase in magnitude in the order CALF-20 < NU-220 < CALF-20M-w < CALF-20M-e (Table 1). To discern the primary factors contributing to the higher CO2 adsorption energies for the latter three MOFs, we examined the van der Waals (vdW) and Coulombic contributions of each atom in the CO<sub>2</sub> molecule with the MOF frameworks. The results are provided in **Table S4**. It can be seen that the total vdW energy consistently surpasses the total Coulombic energy. Although the vdW contribution of each CO<sub>2</sub> oxygen ([0]-C-0 and 0-C-[0]) exceeds that of carbon (0-**[C]-0**), both contributions are found to be favorable (< 0). On the other hand, the Coulombic interactions of the CO<sub>2</sub> carbon atoms with the MOF are favorable, while those of the CO<sub>2</sub> oxygen atoms are unfavorable. This suggests that the CO<sub>2</sub> carbon atoms preferentially form favorable interactions with negatively charged framework atoms like oxygen and nitrogen, and it is the increased Coulombic interaction that makes CO2 adsorption more favorable in CALF-20M-e than CALF-20 (-17.4 versus -8.7 kJ/mol).

Next, the single-component  $CO_2$  and water isotherms for all four sorbents were determined by GCMC simulations. The simulated results for  $CO_2$  at 298 K closely match the experimental isotherms for CALF-20 and NU-220 (Figures S41-S42), and for CALF-20M-w and CALF-20M-e, the simulated isotherms have the same shape as those from experiment, but with higher loadings predicted at higher pressures (Figures 4b and S43). Water isotherms tend to be more difficult to predict, and the agreement between simulation and experiment (Figures S45–S48) is reasonably good, with similar trends as seen in experiment (compare Figure 2d and Figure S49). To elucidate the water-sorbent interactions, we calculated the adsorbate-adsorbate energy, host-adsorbate energy, and total potential energy of all sorbents as a function of RH (Figures S50-S53).

In the case of CALF-20, the water-water interactions increase dramatically around 25% RH, which is also the range where the isotherm rises sharply, suggesting the emergence of a hydrogen bonding network among water molecules (Figure S50). This is also observed in NU-220 (Figure S51) but at even lower RH values (< 20% RH). In contrast, CALF-20M-w and CALF-20M-e demonstrate minimal water-water interactions (as shown in Figures S52-S53), demonstrating that the modifications in pore dimension and shape dramatically impact the ability of water to form hydrogen bonding networks. This observation suggests that methyl functionalization presents a promising opportunity for CALF-20M-w and CALF-20M-e to effectively capture CO<sub>2</sub> under high humidity conditions.

To compare the water network in all frameworks, we visualized the distribution of water molecules in the pores at

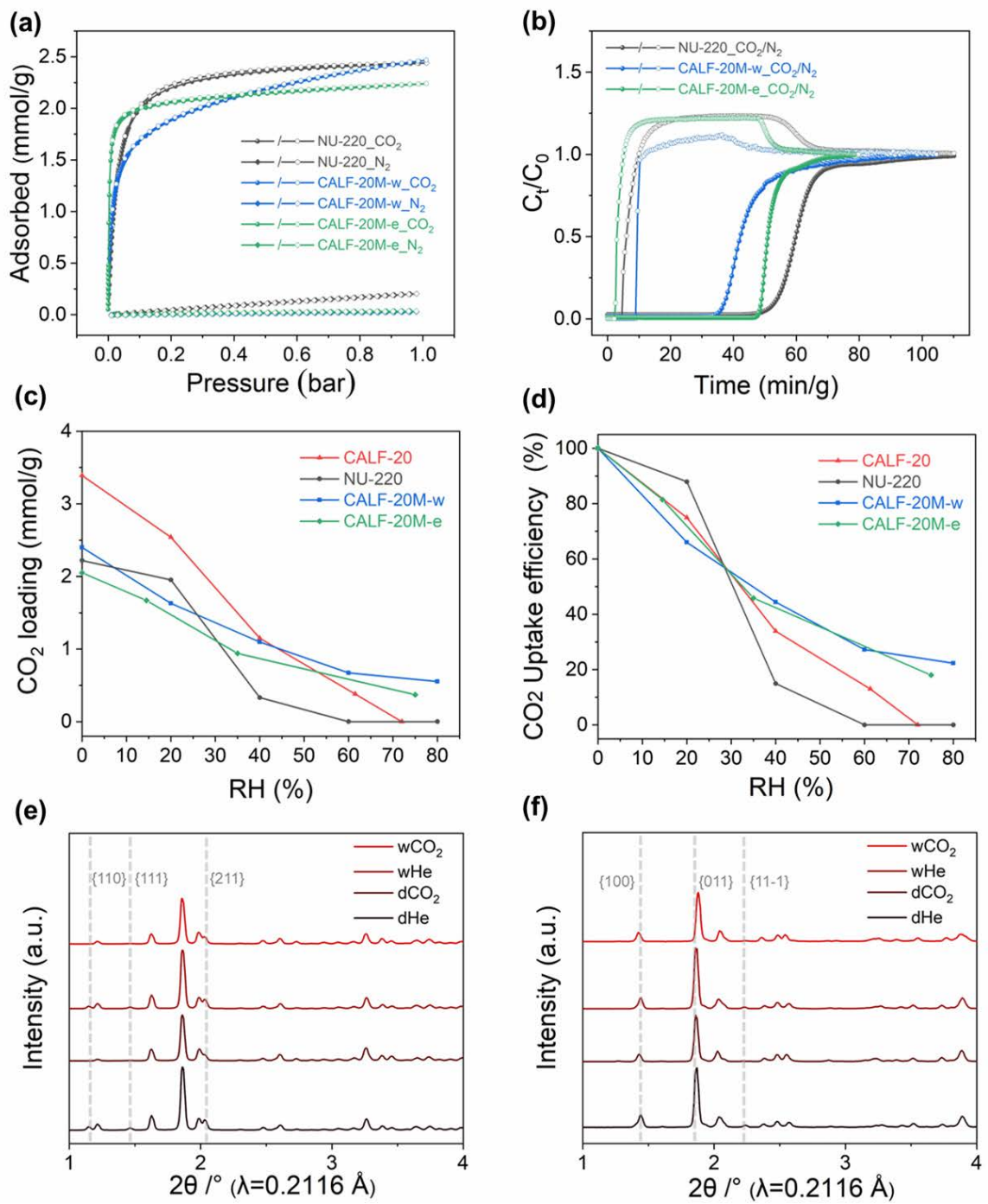


**Figure 5.** (a) CO<sub>2</sub> and N<sub>2</sub> isotherms in **NU-220**, **CALF-20M-w**, and **CALF-20M-e** at 298 K. (b) Experimental breakthrough curves of **NU-220**, **CALF-20M-w** and **CALF-20M-e** with the binary mixture of CO<sub>2</sub>/N<sub>2</sub> (15/85, v/v). The flow rate was set at 5 cc/min, and the experiments were conducted at 1 bar and 298 K. Solid circles represent CO<sub>2</sub> and hollow circles represent N<sub>2</sub>. (c-d) CO<sub>2</sub> captured amount and efficiency under different humidities for CALF-20, **NU-220**, **CALF-20M-w** and **CALF-20M-e**. Data from an *in-situ* gas loading PXRD experiment ( $\lambda$ = 0.2116 Å) on (e) **NU-220** and (f) **CALF-20M-w**. The sample was loaded under dry conditions with dry helium (dHe), dry CO<sub>2</sub> (dCO<sub>2</sub>), and humid conditions (100% RH) with helium (wHe) and humid CO<sub>2</sub> (wCO<sub>2</sub>).

95% RH (**Figures 4c**, **4d**, and **S54**) and quantified the proportion of water molecules that form hydrogen bonds with other water molecules and with the framework (**Figures 4e**, **4f**, **and S55-S56**). The criteria to define a hydrogen bond were an 0-H-0 angle greater than 150° and an 0-H distance less than 2.5 Å.<sup>35</sup> The results show that both CALF-20 and **NU-220** contain a significant proportion of molecules that form two hydrogen bonds with other water molecules, consistent with the conclusion from the water-water potential energy analysis (**Figures S50-S51**). On the other hand,

**CALF-20M-w** and **CALF-20M-e** show very few water molecules forming two hydrogen bonds with other water molecules. Analysis of the hydrogen bonds between water molecules and the framework showed that hydrogen bonding with the oxalate groups was particularly favored, and all four materials have a high fraction of water molecules that form one hydrogen bond with the framework.

Finally, we simulated competitive isotherms with the total pressure fixed at 1 bar, the gas-phase mole fraction of  $CO_2$  fixed at 14%, variable RH, and the balance of the gas phase

as nitrogen. The results in **Figures 4g, 4h and S57-S58** show that the loading of  $CO_2$  in CALF-20 drops dramatically when the humidity exceeds 50% RH, and nearly no adsorption was observed at 75% RH (**Figure 4g**). However, the presence of methyl groups enabled **CALF-20M-w** to retain a  $CO_2$  capacity of  $\sim$ 0.8 mmol/g even when the RH reached 90 % (**Figure 4h**).

# Dynamic Breakthrough and Competitive CO<sub>2</sub> Capture Under Humidity

Inspired by the multicomponent GCMC results, we assessed the CO<sub>2</sub>/N<sub>2</sub> separation performance of NU-220, CALF-20Mw, CALF-20M-e through pure gas isotherms and kinetic experimental breakthrough tests. The pure CO2 and N2 sorption isotherms for the four sorbents were measured at 298 K (Figures 5a and S59) and employed with ideal adsorbed solution theory (IAST) to assess the separation performance. NU-220 shows a somewhat higher selectivity (440 versus 350 at 1 bar) for CO2 over N2 (15/85, v/v) compared to CALF-20 (Figure S60). However, CALF-20M-w and CALF-20M-e displayed negligible single-component N2 uptake at 298 K, suggesting even higher selectivity. Next, we performed dynamic column breakthrough experiments (DCB) to more directly examine the CO<sub>2</sub>/N<sub>2</sub> separation performance for these MOFs. A binary mixture of CO<sub>2</sub>/N<sub>2</sub> with a composition of 15/85 (v/v), representing a typical flue gas composition, was passed through a packed column containing glass beads and the sorbents. All three polymorphs exhibit sharp breakthrough curves in the N<sub>2</sub> profile, indicating rapid breakthrough of N2 (Figure 5b), without noticeable changes after three cycles (Figures S61-S63). In addition, we observed distinct breakthrough retention times for the CO<sub>2</sub> concentration profiles for each MOF. Specifically, the retention times as shown in **Figure 5b** followed the sequence: NU-220 (55 min  $g^{-1}$ )> CALF-20M-e (48 min  $g^{-1}$ )> CALF-**20M-w** (33 min g<sup>-1</sup>). The elution times align closely with the CO<sub>2</sub> adsorbed amount at 0.15 bar, suggesting that the uptake capacity was the primary factor in the retention.

Considering the adsorption energies in Table 1, the relevance of N2 uptake within this study is minor, and preferential adsorption of either CO<sub>2</sub> or H<sub>2</sub>O was indicated in both simulations and experiments, signifying a pronounced CO<sub>2</sub> to N<sub>2</sub> selectivity especially for CALF-20M-w and CALF-**20M-e**. To probe the CO<sub>2</sub> uptake performance for these MOFs in the presence of humidity, we employed an experimental setup involving humid CO2 capture experiments using a flow gas system in which we subjected each sorbent to streams of CO2 with varying RH values (Scheme S1 and setup details in Supporting Information). Specifically, we placed the sorbent samples in a ceramic container and positioned them within a tube furnace. To ensure proper activation, the sorbents were treated with dry nitrogen followed by heating to 413 K before cooling to room temperature for humid CO2 capture experiments. Next, we performed the subsequent analysis using a thermogravimetric analysis instrument equipped with gas chromatography mass spectrometry (TGA-GCMS) to accurately measure the quantity of loaded CO<sub>2</sub>. For desorption experiments, the sorbent samples were heated to 413 K under a continuous flow of Ar as the carrier gas. GC-MS analysis enabled the identification and quantification of the amount of the resulting exhaust gases, which contained CO<sub>2</sub> and H<sub>2</sub>O. Notably, the experimentally quantified amount of CO2 adsorbed is

possibly underestimated compared to the actual amount adsorbed due to the slight loss of  $CO_2$  that occurs during the transfer/mounting of saturated sorbents from the furnace to the TGA-GCMS instrument, which necessitated exposure of the samples to ambient conditions after uncapping. Thus, a large amount of sorbent (>100 mg) was utilized to minimize the effect.

The results in **Figure 5c** illustrate a gradual reduction in the  $CO_2$  adsorption capacity of CALF-20 as the RH increases. Eventually, at an RH level of  $\sim 70\%$ , the  $CO_2$  adsorption capacity approaches zero, and water emerges as the dominant adsorbed species at high RH. A comparable trend was seen in **NU-220**, where there was a marked reduction in  $CO_2$  adsorption at around 60% RH, but it maintained higher capture efficiency below 30% RH (**Figure 5d**). Consequently, **NU-220** proves unsuitable for capturing  $CO_2$  from humid flue gas, as the  $CO_2$  uptake becomes negligible around 60% RH.

On the other hand, the results for CALF-20M-w and CALF-20M-e in Figure 5c and 5d reveal that some CO2 capacity remained even at high humidity levels. Unlike in the case of NU-220, the methyl functional groups in CALF-20M-w and CALF-20M-e efficiently limit the formation of hydrogen bonding networks, as discussed above. These two sorbents exhibit superior CO<sub>2</sub> uptake capacity above 45% and 55% RH, approximately 1.0 and 0.7 mmol/g CO<sub>2</sub>, respectively, despite lower inherent pore volumes compared to that of CALF-20. The large amount of water uptake observed in single-component water isotherms in CALF-20 (Figure 2d) results in a loss of approximately 30% in CO<sub>2</sub> uptake efficiency at 20% RH in the multicomponent measurements. In contrast, CALF-20M-w and CALF-20M-e demonstrate a more gradual decrease in CO<sub>2</sub> capture performance with increasing RH, showing 20% CO<sub>2</sub> uptake capacity at 80% RH. These results are qualitatively consistent with the modeling results (Figures 4h and S58) and suggest that CALF-20M-w and CALF-20M-e provide considerable promise for CO<sub>2</sub> capture from moist flue gas compared to CALF-20 under the same humid conditions.

A potential reason for the difference between the simulated and experimental pure and multicomponent isotherms for CALF-20M-w and CALF-20M-e is structural flexibility of the MOFs (Figures 4b, 4h and S43, S58). Thus, in situ PXRD measurements were carried out with CO<sub>2</sub> sorption to investigate the structural changes during CO<sub>2</sub> capture. The activated sample was loaded under dry conditions with dry helium (dHe), dry CO<sub>2</sub> (dCO<sub>2</sub>), and under humid conditions with humid helium (wHe) and humid CO<sub>2</sub> (wCO<sub>2</sub>) (details in Supporting Information). The PXRD data (Figures 5e-f and S65) is presented for the sample subjected to gas adsorption and desorption cycles, transitioning between dry and humid conditions. We performed a Pawley refinement for the model for **NU-220** to determine the purity (**Figure S64**). Notably, the annotated reflections {110}, {111}, and {211} in NU-220 (Figure 5e) demonstrate diminished intensity, potentially attributable to the CO<sub>2</sub> uptake, signifying an almost instantaneous structural transition that remains reversible. Crucially, the intrinsic order of the MOF remains predominantly unaltered under these conditions, even at elevated RH levels, indicating the rigid structure of NU-220. Subsequently, we performed an analogous in situ PXRD analysis for CALF-20M-w and CALF-20M-e, against the data for helium-loaded samples under dry and humid

conditions. Figure 5f shows the PXRD patterns of CALF-**20M-w** throughout the whole dHe, dCO<sub>2</sub>, wHe, wCO<sub>2</sub> adsorption cycle. During dry and humid CO2 capture, characteristic peaks at 1.86° (annotated reflection {011}) shifted to 1.88°, demonstrating the structural alternation in CALF-20M-w during CO<sub>2</sub> capture (Figure 5f). The observed decrease in intensity of the annotated reflection {11-1} in CALF-20M-w can be attributed to the adsorption of CO<sub>2</sub>. A similar observation was made with the annotated reflection {110} of **CALF-20M-e**, where the peak shifted from 1.85° to 1.87°. (Figure S65). The in situ gas loading experiments successfully demonstrated the structural transition during wCO<sub>2</sub> capture and helped explain the difference between experimental results and simulation for mixture adsorption. For instance, the simulated multicomponent isotherms for CALF-20M-e do not indicate any large changes in CO2 uptake at elevated RH values, which remains at >90% of the initial CO2 uptake, even under 100% RH (Figure S58). In contrast, experimental results indicate CALF-20M-e preserves only ~20% of its initial CO<sub>2</sub> uptake capacity at 80% RH, which is significantly lower than the value predicted by simulation. As for CALF-20M-w, even when accounting for the inherent loss of sequestered CO<sub>2</sub>, it retains 23% of its efficiency experimentally, in contrast to the 57% projected by the modeling. Despite the structural flexibility demonstrated by CALF-20M-w and CALF-20M-e, these experimental results still highlight their great potential for capturing CO<sub>2</sub> from highly humid flue gas.

#### Conclusion

In this work, we demonstrated that incorporating methyl groups into the triazolate linkers affords robust materials better tailored than the related material without methyl groups to capture CO<sub>2</sub> from post-combustion flue gas in the presence of water. Specifically, we synthesized three new MOFs, denoted as NU-220, CALF-20M-w, and CALF-20M-e, from the same metal salt and organic linker precursors but from different solvents. **NU-220** features a different topology than that of CALF-20, whereas CALF-20M-w and CALF-20M-e are isostructural to CALF-20. In all three cases, the presence of methyl groups resulted in significant modifications to the pore size and pore environment. Molecular simulations suggest that the methyl groups sterically hinder the formation of hydrogen bonding networks by water molecules and further repel water molecules from approaching framework Zn-N bonds relative to the non-methylated analogues, supporting the experimentally observed increase in stability in the presence of water for these new MOFs. Humid CO<sub>2</sub> capture experiments confirm that incorporating the methyl group results in a significant improvement in CO2 uptake at high RH values, as CALF-20M-w and CALF-**20M-e** maintain about 20% of their initial CO<sub>2</sub> uptake at 80% RH, whereas CALF-20 loses all of its initial CO2 uptake at this same RH. As a result, CALF-20M-w and CALF-20M-e show promise for CO<sub>2</sub> capture in post-combustion flue gas environments, while NU-220 excels among this series for CO<sub>2</sub> capture in dry or low RH conditions. Overall, this simple design strategy has afforded new adsorbent materials that are better suited for practical CO<sub>2</sub> capture conditions from humid post combustion flue gas streams than CALF-20, overcoming a significant drawback for this CO2 adsorbent and increasing the potential success of this class of physisorbents in carbon capture technologies.

## **ASSOCIATED CONTENT**

**Supporting Information**. Detailed material synthesis and characterization, modeling details, and additional results are available free of charge via the Internet at http://pubs.acs.org.

#### **AUTHOR INFORMATION**

### Corresponding Author

- \* Omar K. Farha, o-farha@northwestern.edu
- \* Randall Q. Snurr, snurr@northwestern.edu

#### Conflicts of Interest

O.K.F. and R.Q.S. have a financial interest in NuMat Technologies, a startup company that is seeking to commercialize MOFs.

#### **Author Contributions**

The manuscript was written through contributions of all authors

### **ACKNOWLEDGMENT**

This work is supported by U.S. Department of Energy (DOE) grant DE-SC0022332. R.Q.S. gratefully acknowledges research support from the National Science Foundation under grant no. 2119433. This research made use of the EPIC facility of Northwestern University's NUANCE Center, which has received support from the Soft and Hybrid Nanotechnology Experimental (SHyNE) Resource (NSF ECCS-2025633). We acknowledge the Integrated Molecular Structure Education and Research Center (IMSERC) at Northwestern University for providing access to equipment for relevant experiments, which has received support from NSF CHE-1048773. We also thank Prof. Sossina M. Haile for her invaluable support in the humid CO2 capture experiments.

### **REFERENCES**

- (1) Wang, Q.; Luo, J.; Zhong, Z.; Borgna, A.  $CO_2$  capture by solid adsorbents and their applications: current status and new trends. *Energy Environ. Sci.* **2011**, *4* (1), 42-55.
- (2) Sanz-Perez, E. S.; Murdock, C. R.; Didas, S. A.; Jones, C. W. Direct Capture of CO<sub>2</sub> from Ambient Air. *Chem. Rev. (Washington, DC, U. S.)* **2016**, *116* (19), 11840-11876.
- (3) Abbasi, T.; Premalatha, M.; Abbasi, S. A. The return to renewables: Will it help in global warming control? *Renewable Sustainable Energy Rev.* **2011**, *15* (1), 891-894.
- (4) Edenhofer, O.; Pichs-Madruga, R.; Sokona, Y.; Seyboth, K.; Kadner, S.; Zwickel, T.; Eickemeier, P.; Hansen, G.; Schlömer, S.; von Stechow, C.; et al. *Renewable Energy Sources and Climate Change Mitigation*; Cambridge University Press, 2011.
- (5) Hills, T.; Leeson, D.; Florin, N.; Fennell, P. Carbon Capture in the Cement Industry: Technologies, Progress, and Retrofitting. *Environ. Sci. Technol.* **2016**, *50* (1), 368-377.
- (6) Erans, M.; Sanz-Pérez, E. S.; Hanak, D. P.; Clulow, Z.; Reiner, D. M.; Mutch, G. A. Direct air capture: process technology, techno-economic and socio-political challenges. *Energy Environ. Sci.* **2022**, *15* (4), 1360-1405.
- (7) Trickett, C. A.; Helal, A.; Al-Maythalony, B. A.; Yamani, Z. H.; Cordova, K. E.; Yaghi, O. M. The chemistry of metal-organic frameworks for CO2 capture, regeneration and conversion. *Nat. Rev. Mater.* **2017**, *2* (8), 17045
- (8) Pardakhti, M.; Jafari, T.; Tobin, Z.; Dutta, B.; Moharreri, E.; Shemshaki, N. S.; Suib, S.; Srivastava, R. Trends in Solid Adsorbent Materials Development for CO<sub>2</sub> Capture. *ACS Appl. Mater. Interfaces* **2019**, *11* (38), 34533-34559.
- (9) Singh, G.; Lee, J.; Karakoti, A.; Bahadur, R.; Yi, J. B.; Zhao, D. Y.; AlBahily, K.; Vinu, A. Emerging trends in porous materials for CO2capture and conversion. *Chemical Society Reviews* **2020**, 49 (13), 4360-4404.

- (10) Kolle, J. M.; Fayaz, M.; Sayari, A. Understanding the Effect of Water on CO<sub>2</sub> Adsorption. *Chem Rev* **2021**, *121* (13), 7280-7345.
- (11) Bose, S.; Sengupta, D.; Malliakas, C. D.; Idrees, K. B.; Xie, H.; Wang, X.; Barsoum, M. L.; Barker, N. M.; Dravid, V. P.; Islamoglu, T.; et al. Suitability of a diamine functionalized metal-organic framework for direct air capture. *Chem Sci* **2023**, *14* (35), 9380-9388.
- (12) Rajendran, A.; Shimizu, G. K. H.; Woo, T. K. The Challenge of Water Competition in Physical Adsorption of CO<sub>2</sub> by Porous Solids for Carbon Capture Applications A Short Perspective. *Adv Mater* **2023**, e2301730. (13) Haghpanah, R.; Nilam, R.; Rajendran, A.; Farooq, S.; Karimi, I. A.
- Cycle synthesis and optimization of a VSA process for postcombustion CO<sub>2</sub> capture. *AIChE Journal* **2013**, *59* (12), 4735-4748.
- (14) Burns, T. D.; Pai, K. N.; Subraveti, S. G.; Collins, S. P.; Krykunov, M.; Rajendran, A.; Woo, T. K. Prediction of MOF Performance in Vacuum Swing Adsorption Systems for Postcombustion  $CO_2$  Capture Based on Integrated Molecular Simulations, Process Optimizations, and Machine Learning Models. *Environmental Science & Technology* **2020**, *54* (7), 4536-4544.
- (15) Bose, S.; Sengupta, D.; Rayder, T. M.; Wang, X. L.; Kirlikovali, K. O.; Sekizkardes, A. K.; Islamoglu, T.; Farha, O. K. Challenges and Opportunities: Metal-Organic Frameworks for Direct Air Capture. *Advanced Functional Materials* **2023**, 2307478.
- (16) Ding, M.; Flaig, R. W.; Jiang, H. L.; Yaghi, O. M. Carbon capture and conversion using metal-organic frameworks and MOF-based materials. *Chem Soc Rev* **2019**, *48* (10), 2783-2828.
- (17) Yu, J.; Xie, L. H.; Li, J. R.; Ma, Y.; Seminario, J. M.; Balbuena, P. B. CO2 Capture and Separations Using MOFs: Computational and Experimental Studies. *Chem Rev* **2017**, *117* (14), 9674-9754.
- (18) Sanz-Perez, E. S.; Murdock, C. R.; Didas, S. A.; Jones, C. W. Direct Capture of CO2 from Ambient Air. *Chem Rev* **2016**, *116* (19), 11840-11876.
- (19) Nugent, P.; Belmabkhout, Y.; Burd, S. D.; Cairns, A. J.; Luebke, R.; Forrest, K.; Pham, T.; Ma, S.; Space, B.; Wojtas, L.; et al. Porous materials with optimal adsorption thermodynamics and kinetics for CO<sub>2</sub> separation. *Nature* **2013**, *495* (7439), 80-84.
- (20) Hu, Z.; Wang, Y.; Shah, B. B.; Zhao, D. CO<sub>2</sub> Capture in Metal-Organic Framework Adsorbents: An Engineering Perspective. *Advanced Sustainable Systems* **2018**, *3* (1), 1800080.
- (21) Belmabkhout, Y.; Guillerm, V.; Eddaoudi, M. Low concentration CO<sub>2</sub> capture using physical adsorbents: Are metal–organic frameworks becoming the new benchmark materials? *Chemical Engineering Journal* **2016**, *296*, 386-397.
- (22) Lin, J. B.; Nguyen, T. T. T.; Vaidhyanathan, R.; Burner, J.; Taylor, J. M.; Durekova, H.; Akhtar, F.; Mah, R. K.; Ghaffari-Nik, O.; Marx, S.; et al. A scalable metal-organic framework as a durable physisorbent for carbon dioxide capture. *Science* **2021**, *374* (6574), 1464-1469.
- (23) Nguyen, T. T. T.; Lin, J.-B.; Shimizu, G. K. H.; Rajendran, A. Separation of  $CO_2$  and  $N_2$  on a hydrophobic metal organic framework CALF-20. *Chemical Engineering Journal* **2022**, 442, 136263.

- (24) Ozin, G. *CALF-20: A carbon capture success story*. Advanced Science News, 2022. <a href="https://www.advancedsciencenews.com/calf-20-acarbon-capture-success-story/">https://www.advancedsciencenews.com/calf-20-acarbon-capture-success-story/</a> (accessed 2023 09/05).
- (25) Ho, C. H.; Paesani, F. Elucidating the Competitive Adsorption of H2O and CO2 in CALF-20: New Insights for Enhanced Carbon Capture Metal-Organic Frameworks. *ACS Appl Mater Interfaces* **2023**, *15* (41), 48287-48295.
- (26) Xu, D.; Xiao, P.; Zhang, J.; Li, G.; Xiao, G.; Webley, P. A.; Zhai, Y. Effects of water vapour on CO<sub>2</sub> capture with vacuum swing adsorption using activated carbon. *Chemical Engineering Journal* **2013**, *230*, 64-72.
- (27) Kemper, J.; Sutherland, L.; Watt, J.; Santos, S. Evaluation and Analysis of the Performance of Dehydration Units for CO<sub>2</sub> Capture. *Energy Procedia* **2014**, *63*, 7568-7584.
- (28) Li, J.; Tharakan, P.; Macdonald, D.; Liang, X. Technological, economic and financial prospects of carbon dioxide capture in the cement industry. *Energy Policy* **2013**, *61*, 1377-1387.
- (29) Reger, D. L.; Pascui, A. E.; Pellechia, P. J.; Smith, M. D. Zinc(II) and Cadmium(II) Monohydroxide Bridged, Dinuclear Metallacycles: A Unique Case of Concerted Double Berry Pseudorotation. *Inorg. Chem.* **2013**, *52* (19), 11638-11649.
- (30) Wei, X.-F.; Miao, J.; Shi, L.-L. Synthesis, Crystal Structure, and Luminescent Property of One 3D Porous Metal-Organic Framework With dmc Topology. *Synth. React. Inorg., Met.-Org., Nano-Met. Chem.* **2016**, *46* (3), 365-369.
- (31) Yu, L.; Xiong, S.; Lin, Y.; Li, L.; Peng, J.; Liu, W.; Huang, X.; Wang, H.; Li, J. Tuning the Channel Size and Structure Flexibility of Metal-Organic Frameworks for the Selective Adsorption of Noble Gases. *Inorg Chem* **2019**, *58* (22), 15025-15028.
- (32) Chen, Z.; Ho, C.-H.; Wang, X.; Vornholt, S. M.; Rayder, T. M.; Islamoglu, T.; Farha, O. K.; Paesani, F.; Chapman, K. W. Humidity-Responsive Polymorphism in CALF-20: A Resilient MOF Physisorbent for CO<sub>2</sub> Capture. *ACS Materials Letters* **2023**, 2942-2947.
- (33) Banerjee, A.; Nandi, S.; Nasa, P.; Vaidhyanathan, R. Enhancing the carbon capture capacities of a rigid ultra-microporous MOF through gate-opening at low CO<sub>2</sub> pressures assisted by swiveling oxalate pillars. *Chem Commun (Camb)* **2016**, *52* (9), 1851-1854.
- (34) Yang, S. Q.; Krishna, R.; Chen, H.; Li, L.; Zhou, L.; An, Y. F.; Zhang, F. Y.; Zhang, Q.; Zhang, Y. H.; Li, W.; et al. Immobilization of the Polar Group into an Ultramicroporous Metal-Organic Framework Enabling Benchmark Inverse Selective  $CO_2/C_2H_2$  Separation with Record  $C_2H_2$  Production. *J Am Chem Soc* **2023**, *145* (25), 13901-13911.
- (35) Zielkiewicz, J. Structural properties of water: comparison of the SPC, SPCE, TIP4P, and TIP5P models of water. *J Chem Phys* **2005**, *123* (10), 104501.

